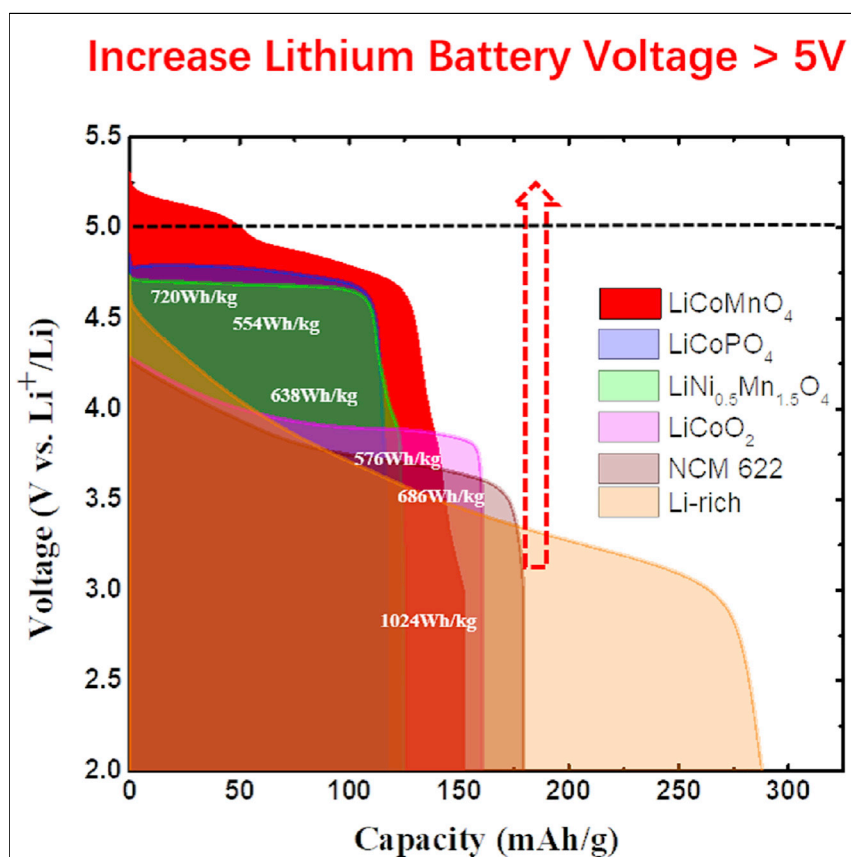


## Article

# Achieving High Energy Density through Increasing the Output Voltage: A Highly Reversible 5.3 V Battery



A 5.5 V high-voltage electrolyte enables both Li-metal and graphite anodes and 5.3 V LiCoMnO<sub>4</sub> cathodes to achieve a high Coulombic efficiency of >99%, opening new opportunity to develop high-energy Li-ion batteries. The design principle for the high voltage and safe electrolytes will greatly benefit the development of next-generation electrochemical energy storage devices. These findings should therefore be of extensive interest to a broad audience working on energy storage technologies, materials, and electrochemistry in general.

Long Chen, Xiulin Fan, Enyuan Hu, ..., Dong Su, Xiaoqing Yang, Chunsheng Wang

cswang@umd.edu

## HIGHLIGHTS

Stable 5.5 V electrolytes enable 5.3 V Li-metal battery and 5.2 V Li-ion battery

Investigate the lithiation-delithiation mechanism of 5.3 V LiCoMnO<sub>4</sub> cathodes

Reveal the correlation between electrolytes and CEI or SEI on electrodes



Chen et al., Chem 5, 896–912  
April 11, 2019 © 2019 Elsevier Inc.  
<https://doi.org/10.1016/j.chempr.2019.02.003>



## Article

# Achieving High Energy Density through Increasing the Output Voltage: A Highly Reversible 5.3 V Battery

Long Chen,<sup>1,5</sup> Xiulin Fan,<sup>1,5</sup> Enyuan Hu,<sup>2,5</sup> Xiao Ji,<sup>1</sup> Ji Chen,<sup>1</sup> Singyuk Hou,<sup>1</sup> Tao Deng,<sup>1</sup> Jing Li,<sup>3</sup> Dong Su,<sup>3</sup> Xiaoqing Yang,<sup>2</sup> and Chunsheng Wang<sup>1,4,6,\*</sup>

## SUMMARY

The energy density of current Li-ion batteries is limited by the low capacity of intercalation cathode, which leaves relatively little room to further improve because the specific capacities of these cathodes approach the theoretical levels. Increasing the cell output voltage is a possible direction to largely increase the energy density of the batteries. Extensive research has been devoted to exploring >5.0 V cells, but only limited advances have been achieved because of the narrow electrochemical stability window of the electrolytes (<5.0 V). Herein, we report a 5.5 V electrolyte (1 M LiPF<sub>6</sub> in fluoroethylene carbonate, bis(2,2,2-trifluoroethyl) carbonate, and hydrofluoroether [FEC/FDEC/HFE] with a Li difluoro(oxalate)borate [LiDFOB] additive) that enables 5.3 V LiCoMnO<sub>4</sub> cathodes to provide an energy density of 720 Wh kg<sup>-1</sup> for 1,000 cycles and 5.2 V graphite||LiCoMnO<sub>4</sub> full cells to provide an energy density of 480 Wh kg<sup>-1</sup> for 100 cycles. The 5.5 V electrolytes provide a large step toward developing high-energy Li batteries.

## INTRODUCTION

Today, higher energy density of rechargeable batteries is becoming much more desired as a result of the increasing demands from the coming 5G communication technology, internet of things (IoT), and electric vehicles (EV). Increasing the energy density of batteries has been at the core of battery technology development. The progress in basic science and engineering has driven the emergence of generations of batteries with an increased energy density from Pb acid to Ni-Cd and Ni-MH and finally to Li ion. The advent of a rechargeable Li-ion battery (LIB) in the 1990s is a milestone in science and technology history because of the remarkable energy density, low self-discharge, and negligible memory effect, which in turn intensively stimulated advances in portable electronic devices. Recent requests for longer battery life in mobile devices have resulted in an urgent demand for extremely high-energy-density batteries. The energy density of Li batteries can be enhanced either by increasing the specific capacity of the electrodes<sup>1–7</sup> or by enhancing the cell voltage.<sup>8–10</sup> After more than 10 years of optimization of electrode materials, the energy density of intercalation chemistry cells with voltage of ≤4.4 V has approached the limit as a result of the limited capacity of batteries with Li transition-metal oxide and phosphate cathodes and graphite anode materials, while the high-energy cells with conversion chemistry (such as sulfur and fluorides) still suffer from less reversibility and poor cycle life.<sup>11</sup> However, the low volumetric energy density of the Li-S battery (~200 Wh L<sup>-1</sup> versus 600 Wh L<sup>-1</sup> for the commercial LiCoO<sub>2</sub> battery) and the serious shuttle reaction block the possible application for the EVs. Alternatively,

## The Bigger Picture

Today, a higher energy density of rechargeable battery is becoming much more desired because of the increasing demands from the coming electric vehicles. Current Li-ion batteries based on intercalation cathode chemistry leave relatively little room to further enhance the energy density because the specific capacities of these cathodes approach the theoretical levels. Increasing the cell output voltage is a possible direction to largely increase the energy density of batteries. Extensive research has been devoted to exploring >5.0 V cells, but only limited advances have been achieved because of the narrow electrochemical stability window of the traditional electrolytes (<5.0 V). Herein, we design a 5.5 V electrolyte (1 M LiPF<sub>6</sub> in FEC/FDEC/HFE with LiDFOB additive) that enables 5.3 V LiCoMnO<sub>4</sub> cathodes to provide an energy density of 720 Wh kg<sup>-1</sup> for 1,000 cycles and 5.2 V graphite||LiCoMnO<sub>4</sub> full cells to provide an energy density of 480 Wh kg<sup>-1</sup> for 100 cycles.

an increase in the cell voltage obtained by using a high-potential cathode paired with a low-potential Li-metal or graphite anode can more effectively enhance the energy density of the Li (ion) battery compared with the strategy of increasing the electrode capacity.<sup>8,12</sup>

In recent years, several “high potential” cathodes with operation potential below 5.0 V have been extensively investigated. Among them, nickel-rich layered oxides ( $\text{LiNi}_{1-x}\text{M}_x\text{O}_2$ ,  $\text{M} = \text{Co}, \text{Mn}$  and  $\text{Al}$ ), Li-rich layered oxides ( $\text{Li}_{1+x}\text{M}_{1-x}\text{O}_2$ ,  $\text{M} = \text{Mn}, \text{Ni}, \text{Co}$ , etc.), spinel oxides, and polyanionic compounds (phosphates, sulfates, silicates, etc.)<sup>8</sup> are the most promising cathodes for high-energy Li-ion batteries. However, the average operation potentials of these cathodes are still lower than 4.5 V. Even for the so-called “5.0 V cathode materials,” such as  $\text{LiNi}_{0.5}\text{Mn}_{1.5}\text{O}_4$  and  $\text{LiCoPO}_4$ , their operation potentials are still only 4.7 V and 4.8 V versus  $\text{Li}^+/\text{Li}$ , respectively. Additionally, no electrolytes can sustain these 4.8 V cathodes for a long cycle life. Very recently, a highly concentrated electrolyte enabled a successful 150 cycles of  $\text{LiNi}_{0.5}\text{Mn}_{1.5}\text{O}_4$ .<sup>13</sup> Current electrolytes suffer severe decomposition on these cathode surfaces when the cathodes are fully charged to a potential above 4.5 V.<sup>14,15</sup> Therefore, there has been no report of a highly reversible >5.0 V Li battery up to now.

Spinel structured  $\text{LiCoMnO}_4$  has a high lithiation-delithiation plateau potential of 5.3 V with a theoretical specific capacity of  $145 \text{ mAh g}^{-1}$ ,<sup>16–18</sup> which is a very promising cathode for a high-energy Li battery. However, no electrolytes can sustain such a high voltage (>5.3 V), although significant efforts have been devoted in the past decades to exploring high voltage Li-ion electrolytes by using highly stable solvents<sup>19–24</sup> and functional additives.<sup>25–28</sup> The best electrolytes only allow  $\text{LiCoMnO}_4$  to be partially lithiated or delithiated up to 75% of the theoretical capacity ( $<110 \text{ mAh g}^{-1}$ ).<sup>29–35</sup> Even worse, the decomposition of the electrolytes will result in a very low Coulombic efficiency (CE) (<80%), limiting the cycle life of  $\text{LiCoMnO}_4$  to fewer than 100 cycles.<sup>29–35</sup> Moreover, most of the high-voltage electrolytes with high oxidation tolerance, such as sulfone- and organic nitrile-based electrolytes, normally suffer from poor reductive stability because of the formation of an unstable solid-electrolyte interphase (SEI) on anodes, resulting in poor cycling stability and a low CE for graphite and Li anodes. These high-voltage electrolytes are rarely deployed in Li-ion or Li-metal batteries.<sup>8</sup> In addition, almost all of the previously reported  $\text{LiCoMnO}_4$  contain  $\text{Mn}^{3+}$  ions inside the spinel lattice  $\text{LiCo}^{3+}\text{Mn}^{4+}\text{O}_4$ .<sup>16–18,29–35</sup> The replacement of  $\text{Co}^{3+}$  by  $\text{Mn}^{3+}$  inevitably results in a voltage plateau at 4.0 V, which significantly reduces the energy density.<sup>18</sup>

Herein, we synthesized a  $\text{Mn}^{3+}$ -free  $\text{LiCoMnO}_4$  cathode material by using a two-step method, as detailed in the [Supplemental Information](#). For the first time, the theoretical capacity of  $\text{LiCoMnO}_4$  was realized with a designed versatile electrolyte. The Li storage mechanism of  $\text{LiCoMnO}_4$  was determined via *ex situ* X-ray absorption spectroscopy (XAS) and *in situ* X-ray diffraction (XRD). The specially designed electrolyte (1 M  $\text{LiPF}_6$  in fluoroethylene carbonate, bis(2,2,2-trifluoroethyl) carbonate, and hydrofluoroether [FEC/FDEC/HFE]) with a LiDFOB additive is stable to 5.5 V for the cathodes and, more importantly, also stable with graphite and Li-metal anodes. Because of the extremely high CEs for the Li metal (>99%), graphite (>99.9%), and  $\text{LiCoMnO}_4$  (99%), we fabricated high-energy batteries with a high voltage of 5.3 V, which offer much higher energy densities than current battery chemistries. The fabricated 5.3 V Li-metal cell ( $\text{Li}||\text{LiCoMnO}_4$ ) delivers an energy density of  $720 \text{ Wh kg}^{-1}$  (based on the cathode) with a capacity retention of >80% for over 1,000 cycles, and the 5.2 V LIB (graphite $||\text{LiCoMnO}_4$ ) provides an energy density of

<sup>1</sup>Department of Chemical and Biomolecular Engineering, University of Maryland, College Park, MD 20742, USA

<sup>2</sup>Chemistry Division, Brookhaven National Laboratory, Upton, NY 11973, USA

<sup>3</sup>Center for Functional Nanomaterials, Brookhaven National Laboratory, Upton, NY 11973, USA

<sup>4</sup>Department of Chemistry and Biochemistry, University of Maryland, College Park, MD 20742, USA

<sup>5</sup>These authors contributed equally

<sup>6</sup>Lead Contact

\*Correspondence: [cswang@umd.edu](mailto:cswang@umd.edu)  
<https://doi.org/10.1016/j.chempr.2019.02.003>

480 Wh kg<sup>-1</sup> (based on both cathode and anode materials) with a capacity retention of >90% for 100 cycles.

## RESULTS AND DISCUSSION

### Electrochemical Stability Window of Versatile Electrolyte (1 M LiPF<sub>6</sub> + 0.02 M LiDFOB in FEC/FDEC/HFE)

Wide electrochemical stability of 1 M LiPF<sub>6</sub> in FEC/FDEC/HFE electrolytes stable to 0.0 V Li-metal or 0.1 V graphite anodes and stable to 5.3 V LiCoMnO<sub>4</sub> cathodes is a prerequisite to achieve high-performance Li||LiCoMnO<sub>4</sub> and graphite||LiCoMnO<sub>4</sub> cells and to investigate the lithiation-delithiation mechanism of LiCoMnO<sub>4</sub>. The philosophy behind our solvent selection consists of 5 major considerations:

- (1) Interphase: all solvent molecules must be fluorinated so that as long as they are involved in Li<sup>+</sup>-solvation structure, they have a chance to oxidize into F-rich cathodic electrolyte interphase (CEI) for LiCoMnO<sub>4</sub> cathode and reduce into SEI for Li and graphite anodes. Because HFE has a very high F content per volume, it was selected as an important component for formation of LiF on anodes.
- (2) Salt solubility: a high dielectric constant component must be present to dissolve Li salt; that is the reason for selecting FEC in this electrolyte system.
- (3) Low viscosity: FDEC and HFE serve as diluents to decrease the viscosity.
- (4) High wettability to separator and electrodes, which is contributed by both FDEC and HFE.
- (5) Stability versus reduction and oxidation: according to density functional theory (DFT) calculations, the HFE component had the highest oxidation stability and produced the most F-rich CEI during the reaction. However, the low Li salt solubility in HFE reduced ionic conductivity, requiring another solvent with high salt solubility. FEC has higher affinity to Li<sup>+</sup> than FDEC or HFE and is the most effective component for the LiPF<sub>6</sub> salt dissociation. However, because of the smallest F content per molecule and the FEC•(-H) ring-opening gas-generation reaction, FEC composition should be low but sufficient for ionic conductivity.

The fluorinated solvents have high oxidation potentials as a result of the strong electron-withdrawing effect of the fluorine atom.<sup>22</sup> In addition, LiF is a good electronic insulator that can block electron leakage through the SEI, thereby preventing continuous electrolyte consumption.<sup>36</sup> LiF is also known to exhibit a high interfacial energy with Li metal,<sup>37</sup> which facilitates Li<sup>+</sup> transport along the interface and promotes the growth of the deposited Li metal in parallel with the Li-metal plane rather than in the vertical direction. These features increase the cycle stability of Li metal. Moreover, some additives applied to the electrolyte system can further enhance the stability of the interphase film of both the cathode and anode.<sup>25–28</sup> For this purpose, an electrolyte (1 M LiPF<sub>6</sub> in an FEC/FDEC/HFE ratio of 2:6:2) with a lithium difluoro(oxalate)borate (LiDFOB) additive was designed and applied in our investigation.

The electrochemical stability of the versatile electrolyte (1 M LiPF<sub>6</sub> + 0.02 M LiDFOB in FEC/FDEC/HFE; see [Experimental Procedures](#) for details) after activation was evaluated using a linear sweep voltammogram (LSV) at a slow scan rate of 0.3 mV/s, comparing it with the LSV curves of the conventional carbonate electrolyte (1 M LiPF<sub>6</sub> in ethylene carbonate and dimethyl carbonate [EC/DMC]) at the same scan rate. As shown in [Figures S1A and S1C](#), the oxidation current of this electrolyte

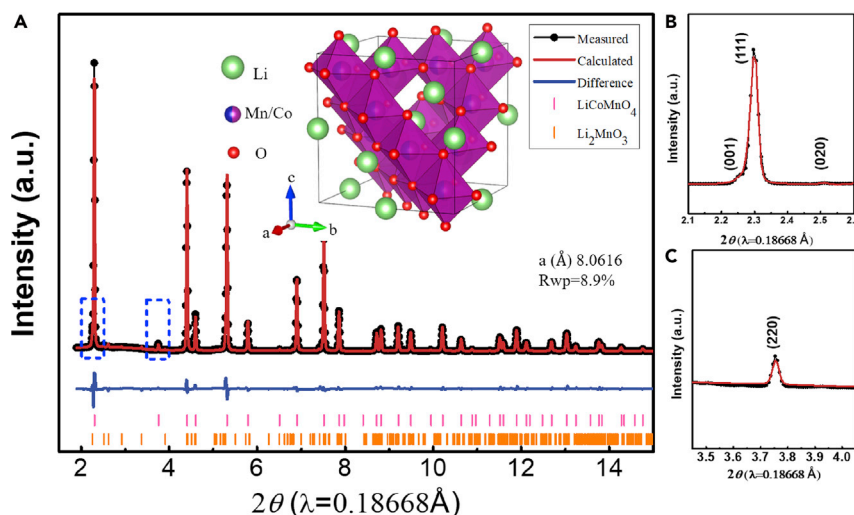


**Figure 1. Structure Analysis of As-Prepared LiCoMnO<sub>4</sub>**

(A) Crystal structure (inset) and X-ray diffraction patterns with Rietveld refinement. The weight percent fractions from structural refinements are as follows: 93% LiCoMnO<sub>4</sub> and 7% Li<sub>2</sub>MnO<sub>3</sub>.

(B) Excerpt of data from 2.1° to 2.6° in 2θ.

(C) Excerpt of data from 3.45° to 4.05° in 2θ.

during the anodic scan is extremely small up to 6.0 V versus Li<sup>+</sup>/Li, while a rapid increase in oxidation current is observed for the conventional carbonate electrolyte at potentials above 4.6 V. In addition, this electrolyte also shows much higher stability for the reduction reaction than the conventional carbonate electrolyte, as demonstrated in Figures S1B and S1D.

### Characterization, Electrochemical Behavior, and Reaction Mechanism of LiCoMnO<sub>4</sub> Synthesized by a Two-Step Method

Using the conventional solid-state reaction method, it is very hard to synthesize the LiCoMnO<sub>4</sub> with uniformly distribute the Co and Mn in the atomic level, which is essential for elimination of the Mn<sup>3+</sup> in the LiCoMnO<sub>4</sub>. Here, the homogeneous LiCoMnO<sub>4</sub> was synthesized by a two-step method. First, we synthesized the precursor of MnCoO<sub>x</sub> by using a hydrothermal procedure, which enabled the Mn and Co elements to be homogeneously distributed at the atomic level. Then, we used homogeneous MnCoO<sub>x</sub> as a precursor to further react with Li<sub>2</sub>CO<sub>3</sub> at 800°C in an O<sub>2</sub> atmosphere to form homogeneous LiCoMnO<sub>4</sub>. The XRD pattern of the LiCoMnO<sub>4</sub> powders showed that LiCoMnO<sub>4</sub> has a cubic Fd $\bar{3}$ m spinel structure (Figure 1A). Detailed structural information of LiCoMnO<sub>4</sub> is shown in Table S1 and illustrated in the inset of Figure 1A. Generally, LiCoMnO<sub>4</sub> shows a typical spinel structure with the space group of Fd $\bar{3}$ m. Cubic close-packed oxygen anions constitute the sub-lattice, in which transition metals occupy octahedral 16d sites and Li occupies tetrahedral 8a sites.<sup>29</sup> In such a framework, Li ions can be extracted and inserted reversibly through three-dimensional pathways made by the interconnected 8a tetrahedral sites and vacant 16c octahedral sites. The relatively strong (220) peak indicates some transition-metal occupation at tetrahedral 8a sites<sup>38</sup> (Figure 1C), and the occupancy was quantitatively determined to be approximately 8% by Rietveld refinement. The small peaks at 2.25° and 2.52° were identified to be the (001) and (020) peaks of Li<sub>2</sub>MnO<sub>3</sub>, respectively (Figures 1A and 1B). Quantitative phase analysis by Rietveld refinement indicated that 7 wt % Li<sub>2</sub>MnO<sub>3</sub> exists in LiCoMnO<sub>4</sub>.



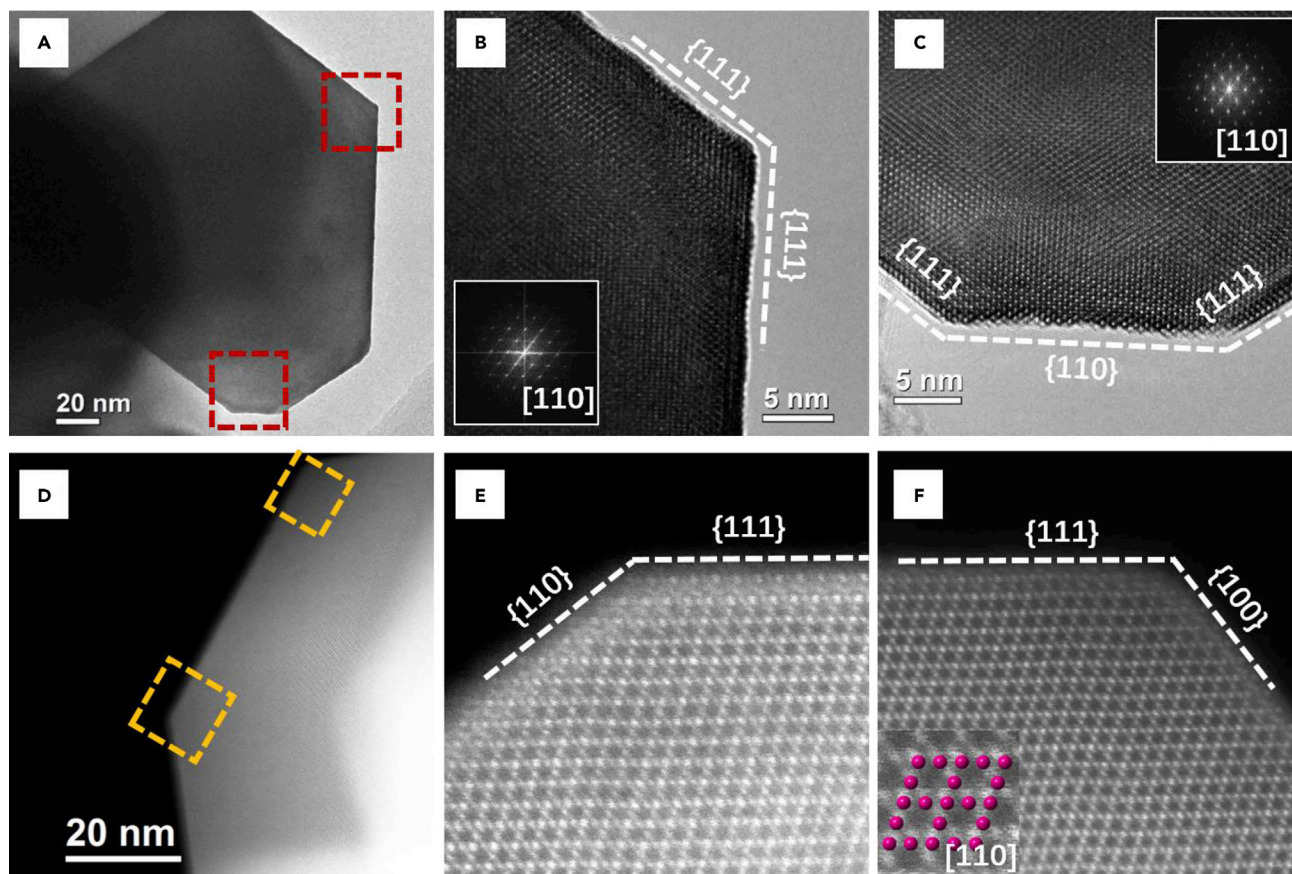


**Figure 2. HRTEM and HR-HAADF-STEM Results of As-Prepared LiCoMnO<sub>4</sub>**

(A) High-resolution TEM image of a whole particle.

(B and C) High-resolution TEM images of the bottom left (B) and top right (C) red dashed areas of the LiCoMnO<sub>4</sub> surface region in (A), where the fast Fourier transform (FFT) patterns in the insets show the [110] zone axis of a spinel structure.

(D) HAADF-STEM image of a whole particle.

(E and F) HR-HAADF-STEM images of bottom left (E) and top right (F) yellow dashed regions of LiCoMnO<sub>4</sub> in (D), where the inset shows the atomic model of the transition-metal atom (Co or Mn) along the [110] zone axis.

Scanning electron microscope (SEM) images showed that LiCoMnO<sub>4</sub> particles have a spherical morphology with a particle size of approximately 5  $\mu\text{m}$  and are primarily aggregates of the LiCoMnO<sub>4</sub> particles with a size of 100–200 nm (Figure S2). Co, Mn, and O elements are homogeneously distributed in LiCoMnO<sub>4</sub>, as demonstrated by the elemental mapping (Figure S3). The high-resolution transmission electron microscopy (HRTEM) and the high-resolution high-angle annular dark-field scanning transmission electron microscopy (HAADF-STEM) results (Figure 2) further revealed the crystalline structure of the LiCoMnO<sub>4</sub> spinel oxide. Along the [110] zone axis, it could be determined that {100}, {110}, and {111} facets are presented. In addition, in the HAADF-STEM images in Figures S4 and S5, the existence of a small amount of Li<sub>2</sub>MnO<sub>3</sub> phase can also be identified in the blue dashed region. However, as shown in Figure S4, the Mn and Co are almost overlapped, and only a small region marked by dashed blue is Li<sub>2</sub>MnO<sub>3</sub>, demonstrating that the proportion of Li<sub>2</sub>MnO<sub>3</sub> in the LiCoMnO<sub>4</sub> is very small, which is in line with the result in Figure 1. The quantitative phase analysis by Rietveld refinement indicated that only 7 wt % Li<sub>2</sub>MnO<sub>3</sub> exists in LiCoMnO<sub>4</sub>. According to the scanning transmission electron microscopy-electron energy loss spectroscopy (STEM-EELS) mapping images (Figures S5B–S5E), the

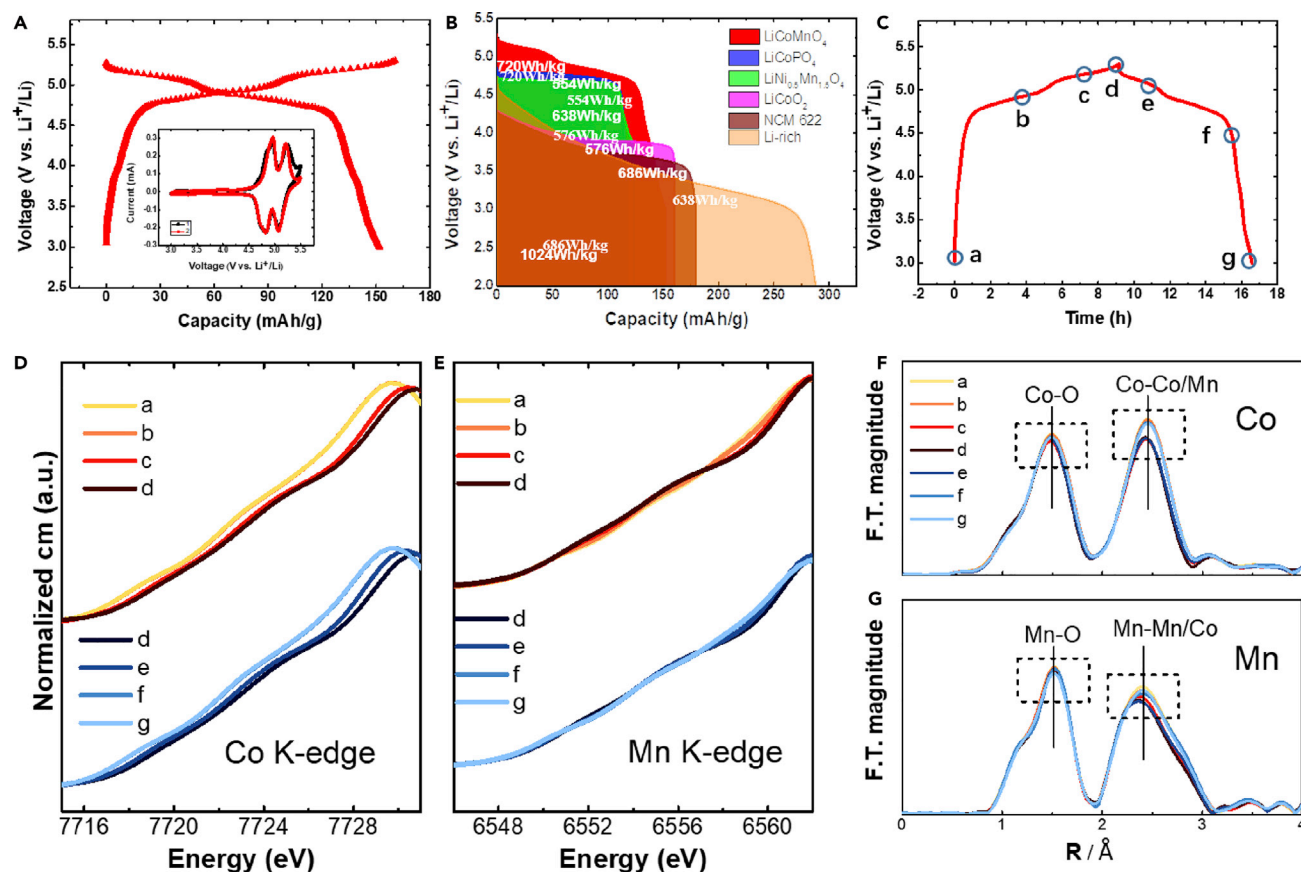


**Figure 3. Electrochemical Performance and Li-Driven Structure Behavior of  $\text{LiCoMnO}_4$**

(A) Galvanostatic charge-discharge profile of  $\text{LiCoMnO}_4$  at a current rate of  $0.1 \text{ A g}^{-1}$  (calculated on the basis of the activated material) between 3 and 5.3 V. The inset is the first two cyclic voltammetry (CV) curves of  $\text{LiCoMnO}_4$ , the scan rate is  $0.3 \text{ mV s}^{-1}$ , and the voltage window is 3–5.5 V.

(B) The discharge profiles and energy density of several high voltage cathode materials ( $\text{LiCoMnO}_4$ ,  $\text{LiCoPO}_4$ ,  $\text{LiNi}_{0.5}\text{Mn}_{1.5}\text{O}_4$ ,  $\text{LiCoO}_2$ , and NCM 622 [ $\text{LiNi}_{0.6}\text{Co}_{0.2}\text{Mn}_{0.2}\text{O}_2$ ] and Li-rich material [ $0.5\text{Li}_2\text{MnO}_3 \cdot 0.5\text{LiMn}_{1/3}\text{Ni}_{1/3}\text{Co}_{1/3}\text{O}_2$ ]), where the current rate is  $0.1 \text{ A g}^{-1}$  (calculated on the basis of the activated material).

(C) First galvanostatic charge-discharge profile of as-prepared  $\text{LiCoMnO}_4$  at a current rate of  $0.02 \text{ A g}^{-1}$  within the voltage window of 3–5.3 V. The regions a–g correspond to different charge-discharge states of  $\text{LiCoMnO}_4$  for XANES and EXAFS tests: a, pristine; b, 4.9 V; c, 5.2 V; d, 5.3 V; e, 5.1 V; f, 4.5 V; g, 3.0 V.

(D) Co K-edge XANES spectra of  $\text{LiCoMnO}_4$  in different charge and discharge states.

(E) Mn K-edge XANES spectra of  $\text{LiCoMnO}_4$  in different charge and discharge states.

(F) Fourier transform of  $k^3$ -weighted EXAFS patterns for the Co K-edge of  $\text{LiCoMnO}_4$  in different charge and discharge states.

(G) Fourier transform of  $k^3$ -weighted EXAFS patterns for the Mn K-edge of  $\text{LiCoMnO}_4$  in different charge and discharge states.

blue dashed region indicates the  $\text{Li}_2\text{MnO}_3$  phase, and the other part is the  $\text{LiCoMnO}_4$  phase; therefore, two phases of  $\text{LiCoMnO}_4$  and  $\text{Li}_2\text{MnO}_3$  coexist in a single particle. Figure S5 was intentionally focused on a  $\text{Li}_2\text{MnO}_3$ -rich region to highlight its presence.

The galvanostatic charge-discharge profile of  $\text{LiCoMnO}_4$  is shown in Figure 3A, and two slope plateaus can be identified upon charging and discharging at approximately 5.0–5.3 and 4.7–4.9 V, respectively. The characteristic plateau at 4.0 V due to  $\text{Mn}^{3+}$  is almost undetectable in homogeneous  $\text{LiCoMnO}_4$ , which is in sharp difference to the  $\text{LiCoMnO}_4$  synthesized using the conventional solid-state reactions, for which a long 4.0 V plateau always exists.<sup>18</sup> The elimination of the 4.0 V plateau is also confirmed by cyclic voltammetry (CV) (inset in Figure 3A).  $\text{LiCoMnO}_4$  in this highly stable 5.5 V electrolyte delivers a reversible specific capacity of  $152 \text{ mAh g}^{-1}$ , which

is even higher than the theoretical specific capacity ( $145 \text{ mAh g}^{-1}$ ) of  $\text{LiCoMnO}_4$ . The presence of 7%  $\text{Li}_2\text{MnO}_3$  (Figures 1 and S5) in the  $\text{LiCoMnO}_4$  particle can probably be responsible for the extra capacity. The embedded  $\text{Li}_2\text{MnO}_3$  in the  $\text{LiCoMnO}_4$  matrix endows high reversibility for lithiation and delithiation.  $\text{Li}_2\text{MnO}_3$  can provide a high discharge capacity of over  $200 \text{ mAh g}^{-1}$  after a high voltage ( $>4.5 \text{ V}$  versus  $\text{Li}^+/\text{Li}$ ) activation process.<sup>39–41</sup> Such a high specific capacity of  $152 \text{ mAh g}^{-1}$  and a high average discharge voltage of  $4.8 \text{ V}$  at a current of  $100 \text{ mA g}^{-1}$  enable the  $\text{LiCoMnO}_4$  to deliver a high energy density of  $720 \text{ Wh kg}^{-1}$ , which is much higher than the densities of other high voltage cathodes, including  $\text{LiNi}_{0.5}\text{Mn}_{1.5}\text{O}_4$  ( $576 \text{ Wh kg}^{-1}$ ),  $\text{LiCoPO}_4$  ( $554 \text{ Wh kg}^{-1}$ ), commercial  $\text{LiCoO}_2$  ( $638 \text{ Wh kg}^{-1}$ ), and intensively investigated Ni-rich  $\text{LiNi}_{0.6}\text{Co}_{0.2}\text{Mn}_{0.2}\text{O}_2$  ( $686 \text{ Wh kg}^{-1}$ , NMC622) (Figure 3B). Although the energy density of the Li-rich cathode ( $1,024 \text{ Wh kg}^{-1}$ ) is higher than that of  $\text{LiCoMnO}_4$ , the gradual potential-drop of Li-rich cathode with charge-discharge cycles reduce the energy density.<sup>8</sup> The electrochemical behavior of  $\text{LiCoMnO}_4$  in a conventional carbonate electrolyte ( $1 \text{ M LiPF}_6$  in EC/DMC) was also evaluated by galvanostatic charging and discharging and LSV. As shown in Figure S6A, only very small amount of Li can be extracted from  $\text{LiCoMnO}_4$  during linear sweep to the high potential because of the serious oxidation of the conventional carbonate electrolyte before Li-ion extraction from the  $\text{LiCoMnO}_4$  structure, as evidenced by the long electrolyte oxidation plateau ( $1,300 \text{ mAh g}^{-1}$ ) at  $5.0 \text{ V}$  and low lithiation capacity of  $<100 \text{ mAh g}^{-1}$  in the galvanostatic charge-discharge curve (Figure S6B). A discharge capacity of  $<100 \text{ mAh g}^{-1}$  for  $\text{LiCoMnO}_4$  in conventional carbonate electrolytes was also reported before.<sup>32–35</sup> The incomplete lithiation and delithiation of  $\text{LiCoMnO}_4$  in conventional carbonate electrolytes prevents the possible commercialization of the  $\text{LiCoMnO}_4$  cathode and the detailed revelation of the lithiation-delithiation mechanism of  $\text{LiCoMnO}_4$ .

The complete lithiation and delithiation of  $\text{LiCoMnO}_4$  is attributed to the formation of robust CEI on  $\text{LiCoMnO}_4$  cathodes. The composition of the CEI formed by oxidation of the electrolyte ( $1 \text{ M LiPF}_6 + 0.02 \text{ M LiDFOB}$  in FEC/FDEC/HFE) at a high potential was investigated. The composition of the CEI on the  $\text{LiCoMnO}_4$  electrode in this electrolyte was characterized by X-ray photoelectron spectroscopy (XPS) (Figure S7). According to the atomic concentration (at. %) of elements of the CEI on the cycled  $\text{LiCoMnO}_4$  electrode, the major elements are carbon (C, 52.97%), fluorine (F, 22.34%), and oxygen (O, 18.96%) (Figure S7B). In the C 1s XPS spectra, the C–O–C bond ( $286.3 \text{ eV}$ ) and  $-\text{CO}_2$  bond ( $289.2 \text{ eV}$ ) indicate the presence of C–O compounds in CEI (Figure S7C). This is probably due to the decomposition of the oxalate moiety in LiDFOB.<sup>27</sup> In addition, in the B 1s XPS spectra, the peak at  $192.8 \text{ eV}$  can be attributed to boron bonded to fluorine (B–F), which also confirms that compounds with the B–F moiety from decomposition of the LiDFOB additive are part of the CEI components on the surface of the cycled  $\text{LiCoMnO}_4$  electrode (Figure S7D). Moreover, the F 1s XPS spectra also exhibit a peak at  $685.2 \text{ eV}$ , corresponding to the Li–F bond (Figure S7E); this component of the CEI can be attributed to the decomposition of LiDFOB and the fluorinated solvent. The peak with a much higher intensity at  $687.8 \text{ eV}$  can be attributed to the C–F bond from the C–F species in the CEI and binder polyvinylidene fluoride (PVDF) (Figure S8). In addition, to unveil the role of LiDFOB in the CEI, we compared the CEI composition of cycled  $\text{LiCoMnO}_4$  cathodes in the electrolytes with and without LiDFOB additives by XPS. As shown in Figure S9C, the relative intensities of the C–C bond and C–H bond are much higher than the one with LiDFOB additives (Figure S10). This is probably due to more decomposition of the solvent without the protective of LiDFOB decomposition products. Therefore, the solvent suffers more severe decomposition without the protective of LiDFOB (Figures S9 and S10). Moreover, to further reveal



the CEI formation process, we also used XPS to characterize the composition of CEI on  $\text{LiCoMnO}_4$  electrode with lithium polyacrylate (LiPAA) as a binder to exclude the possible interference of fluorinated PVDF after 0, 2, and 100 cycles (Figures S11–S13). In the C 1s XPS spectra, the C–F<sub>3</sub> bond was observed in the 100<sup>th</sup> cycles but was absent in the 2<sup>nd</sup> cycle. In the F 1s XPS spectra, the relative intensity of the Li–F bond at 685.2 eV was much higher than the C–F in the 2<sup>nd</sup> cycle. In sharp contrast, the relative intensity of the C–F bond after 100 cycles was much higher than that of the Li–F bond in the F 1s XPS spectra (Figure S14). On the basis of these results, it can be concluded that during the first several cycles, the CEI mostly comes from the decomposition of LiDFOB. Upon further cycling, the decomposition of fluorinated solvents gradually dominates the following cycles. According to the XPS results, the CEI on the surface of the cycled  $\text{LiCoMnO}_4$  electrode in this electrolyte has a very complicated composition. These CEI components are electric insulators, thereby blocking electron leakage through the CEI layer, which can prevent additional electrolyte decomposition. This enables the  $\text{LiCoMnO}_4$  electrode to exhibit great cycle stability and an extremely high CE. The evolution of the bonding and valence of transition-metal ions in  $\text{LiCoMnO}_4$  at different lithiation-delithiation stages marked in Figure 3C was analyzed by *ex situ* XAS that included both X-ray absorption near edge structure (XANES) and extended X-ray absorption fine structure (EXAFS). The XANES data in Figure 3D show that as Li ions are extracted during the charging process (regions a–d), the Co K-edge XANES spectra continuously shift toward a higher energy, suggesting an increase in the oxidation state of Co. In the discharge process (regions e–g), the Co K-edge XANES spectra shift back to the pristine energy state, indicating the reversible reduction of Co in the structure. In contrast, the Mn K-edge XANES spectra show no shift during the entire charge-discharge process (regions a–g, Figure 3E), which suggests that Mn does not change its valence state.

The above XANES spectra of the Co and Mn K-edges confirm that the voltage plateau in the lithiation and delithiation of  $\text{LiCoMnO}_4$  is only attributed to  $\text{Co}^{3+}/\text{Co}^{4+}$ . For the Fourier transform of  $k^3$ -weighted EXAFS patterns in Figures 3F and 3G, the main peaks located at  $\sim 1.5$  and  $\sim 2.4$  Å are associated with the metal-oxygen interaction in the first coordination shell and the metal-metal interaction in the second coordination shell, respectively. The peak positions differ from the real bond length by approximately 0.4 Å because of the phase shift. During the entire charge-discharge process, the positions of the Co–O peak change slightly, indicating a moderate bond length change despite oxidation and reduction on Co. This is probably due to the small size difference between  $\text{Co}^{3+}$  (0.545 Å) and  $\text{Co}^{4+}$  (0.53 Å). The intensity of the peak for the FT EXAFS spectra is determined by two factors: the coordination number and the degree of disorder around the central atom.<sup>42,43</sup> The intensities of the Co–Co/Mn and Mn–Mn/Co peaks are reduced in the high voltage regions (a–d), which suggests significant local structural distortion (more disorder) upon oxidation of  $\text{Co}^{3+}$  ions. During the discharging process (e–g), the intensities of both the Co–Co/Mn and Mn–Mn/Co peaks increase back to almost the original state, indicating that the structure is totally reverted. These XANES and EXAFS spectra confirm the high reversibility of  $\text{LiCoMnO}_4$  during the charging-discharging process.

The dynamic evolution of the phase and structure of  $\text{LiCoMnO}_4$  during the lithiation-delithiation process was monitored by operando XRD measurement. Figure 4 shows selected regions of *in situ* XRD patterns collected during the charge-discharge cycle. Overall, all Bragg peaks exhibit a continuous shift during the entire charge-discharge process, indicating the contraction and expansion of the unit cells of the cubic phase

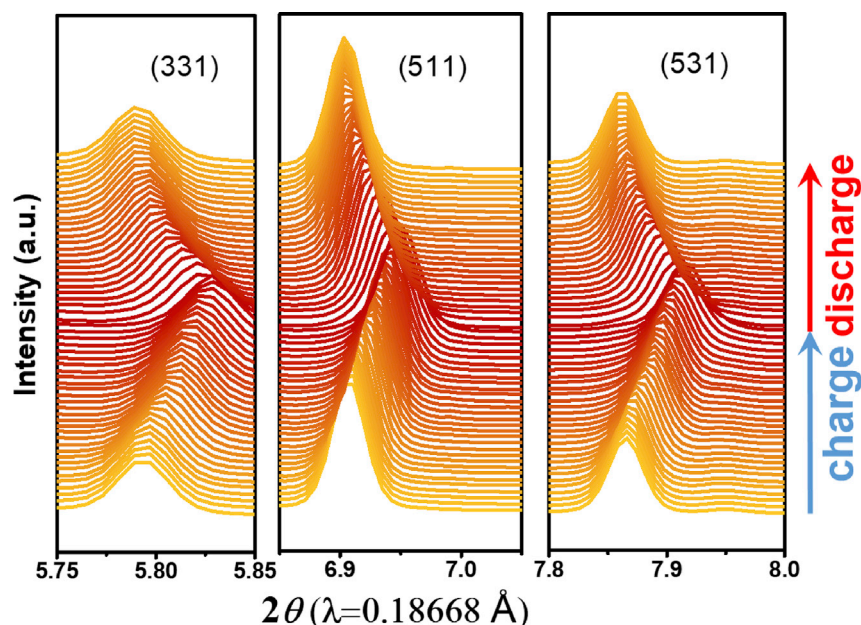


**Figure 4.** *In situ* XRD of LiCoMnO<sub>4</sub>

Selected regions of *in situ* XRD patterns of LiCoMnO<sub>4</sub> collected during the charge-discharge cycle. The operando cell was charged and discharged between 5.3 and 3.0 V at a current rate of C/5.

during Li extraction and insertion. It can be clearly seen that Li extraction and reinsertion occur via a solid-solution mechanism with only one phase over the entire voltage range, as has already been determined by electron paramagnetic resonance (EPR) results before.<sup>44</sup> Such a reaction mechanism is different from other spinel systems, such as LiMn<sub>2</sub>O<sub>4</sub> and LiNi<sub>0.5</sub>Mn<sub>1.5</sub>O<sub>4</sub>, which undergo a two-phase reaction. This can be understood by considering the size difference between various valent cations. For Mn, changing from Mn<sup>3+</sup> (0.645 Å) to Mn<sup>4+</sup> (0.53 Å) would induce a cation size change of 0.115 Å; for Ni, changing from Ni<sup>3+</sup> (0.56 Å) to Ni<sup>4+</sup> (0.48 Å) would induce a size change of 0.08 Å. In contrast, oxidizing Co from Co<sup>3+</sup> (0.545 Å) to Co<sup>4+</sup> (0.53 Å) would only induce a size change of 0.015 Å.<sup>45</sup> Such a small cation size variation greatly favors the formation of a solid solution against two-phase separation given that the latter normally occurs when two phases have significantly different lattice parameters (caused by different cation sizes). As will be shown below, such a solid-solution reaction mechanism is beneficial for the rate capability of this material. Compared with the previous *in situ* XRD results of these materials,<sup>34</sup> the incomplete lithiation and delithiation of LiCoMnO<sub>4</sub> cathode (specific capacity < 110 mAh g<sup>-1</sup>) in conventional electrolyte make it impossible to illustrate the complete lithiation-delithiation mechanism of it.

#### Electrochemical Performance of a 5.3 V Li||LiCoMnO<sub>4</sub> Full Cell

The electrochemical performance of the Li-metal anode in the electrolyte (1 M LiPF<sub>6</sub> + 0.02 M LiDFOB in FEC/FDEC/HFE) was evaluated before a Li||LiCoMnO<sub>4</sub> full cell was tested. The reversibility of Li-metal plating and stripping in this electrolyte was evaluated with a Cu||Li half-cell. The voltage profiles of Li-metal plating and stripping on a Cu current collector showed a small over-potential of approximately 60 mV and long cycling stability at the current density of 0.5 mA cm<sup>-2</sup> (Figure 5A). The CE for plating and stripping reached >99% (Figure 5B), which is much higher than that in the conventional diluted electrolyte (~80%).<sup>46</sup> The high CE of Li plating and stripping in our versatile electrolyte was due to the formation of a LiF-rich SEI

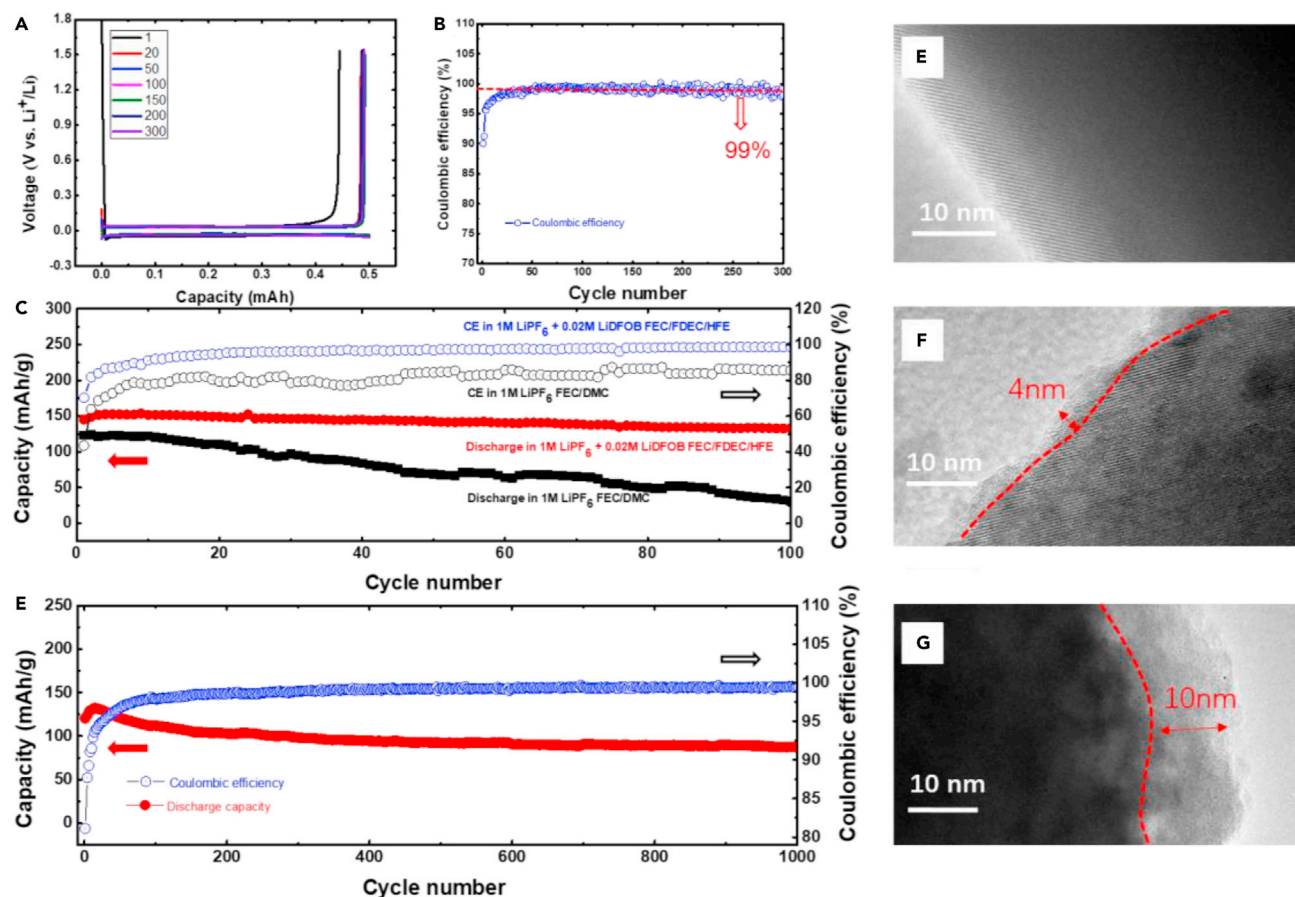


**Figure 5. Electrochemical Performance of a Li||LiCoMnO<sub>4</sub> Cell and TEM Images of the LiCoMnO<sub>4</sub> Electrode after Cycling**

(A) Voltage profiles for Li-metal plating and stripping on a Cu working electrode cycled in the electrolyte 1 M LiPF<sub>6</sub> + 0.02 M LiDFOB in FEC/FDEC/HFE at a current density of 0.5 mA cm<sup>-2</sup>.  
 (B) Coulombic efficiency for Li plating and stripping cycled in the electrolyte 1 M LiPF<sub>6</sub> + 0.02 M LiDFOB in FEC/FDEC/HFE at a current of 0.5 mA cm<sup>-2</sup>.  
 (C) Cycle performance and Coulombic efficiency of the Li||LiCoMnO<sub>4</sub> cell with the electrolyte 1 M LiPF<sub>6</sub> + 0.02 M LiDFOB in FEC/FDEC/HFE and an FEC-based electrolyte (1 M LiPF<sub>6</sub> in FEC/DMC) at a current rate of 0.1 A g<sup>-1</sup> (calculated on the basis of the cathode activated material) between 3 and 5.3 V.  
 (D) Cycle performance of the Li||LiCoMnO<sub>4</sub> cell with the electrolyte 1 M LiPF<sub>6</sub> + 0.02 M LiDFOB in FEC/FDEC/HFE at the current rate of 1 A g<sup>-1</sup> (calculated on the basis of the cathode activated material) between 3 and 5.3 V.  
 (E) TEM image of the fresh LiCoMnO<sub>4</sub>.  
 (F) TEM image of the LiCoMnO<sub>4</sub> cycled in the electrolyte (1 M LiPF<sub>6</sub> + 0.02 M LiDFOB in FEC/FDEC/HFE).  
 (G) TEM image of the LiCoMnO<sub>4</sub> cycled in FEC-based electrolyte (1 M LiPF<sub>6</sub> in FEC/DMC).

(Figure S15), which was also confirmed by Suo in a highly concentrated electrolyte system.<sup>13</sup> The versatile dilute electrolyte reported here has wider electrochemical stability window than the highly concentrated electrolyte.<sup>13</sup>

The cycling performance of the Li||LiCoMnO<sub>4</sub> full cell in this electrolyte (1 M LiPF<sub>6</sub> + 0.02 M LiDFOB in FEC/FDEC/HFE) was compared with that of the Li||LiCoMnO<sub>4</sub> cell in FEC-based electrolyte (1 M LiPF<sub>6</sub> in FEC and DMC [FEC/DMC]) at a current rate of 0.1 A g<sup>-1</sup>. The FEC electrolyte (1 M LiPF<sub>6</sub> in FEC/DMC) has been considered one of the best electrolytes for high-voltage cathodes<sup>23</sup> and has been used for Li||LiNi<sub>0.5</sub>Mn<sub>1.5</sub>O<sub>4</sub> cells (4.7 V) and Li||LiCoPO<sub>4</sub> cells (4.8 V). Therefore, the FEC electrolyte was selected as a control electrolyte for 5.3 V Li||LiCoMnO<sub>4</sub> cells. As shown in Figure 5C, the first discharge capacity of LiCoMnO<sub>4</sub> at 0.1 A g<sup>-1</sup> in the FEC-based electrolyte was only approximately 123 mAh g<sup>-1</sup> and quickly decayed to less than

50 mAh g<sup>-1</sup> after 100 charge-discharge cycles (Figures 5C and S16), whereas the first discharge capacity of LiCoMnO<sub>4</sub> in the functional highly stable electrolyte designed here reached 145 mAh g<sup>-1</sup> and retained 90% of the initial capacity after 100 charge-discharge cycles at the same current of 0.1 A g<sup>-1</sup>. An extended cycle stability test at a high current of 1 A g<sup>-1</sup> showed that the Li||LiCoMnO<sub>4</sub> cell in this electrolyte could retain approximately 80% of its initial capacity even after 1,000 cycles (Figure 5D). The slight capacity decay came from the plateau above 5.0 V, which was probably due to the high over-potential from a thick CEI after long cycles (Figure S17). Such a long cycle life has never been reported for any >5 V batteries before. The CE of Li||LiCoMnO<sub>4</sub> in the first cycle was 71% and increased to 99% after 20 cycles (Figure 5C). In sharp contrast, the initial CE of the Li||LiCoMnO<sub>4</sub> cell in the FEC/DMC electrolyte was only 46% and remained below 85% over the entire 100 cycles. The low cycling CE of Li||LiCoMnO<sub>4</sub> in the FEC/DMC electrolyte demonstrated that 1 M LiPF<sub>6</sub> in FEC/DMC could not form a robust SEI on the Li anode or a robust CEI on LiCoMnO<sub>4</sub>. The continuous decomposition of LiPF<sub>6</sub> in FEC/DMC on the low-potential Li-metal anode and high-potential LiCoMnO<sub>4</sub> cathode increased the interphase resistance, resulting in quick capacity decay of the Li||LiCoMnO<sub>4</sub> cell in the charge-discharge cycles. Transmission electron microscopy (TEM) (Figures 5E–5G) and electrochemical impedance spectroscopy (EIS) (Figure S18) results of the LiCoMnO<sub>4</sub> electrode after 100 cycles confirmed that the CEI formed in FEC/FDEC/HFE electrolyte designed here was much thinner and less resistive than that formed in FEC/DMC electrolytes. In addition, we compared the cycle performance of Li||LiCoMnO<sub>4</sub> cells in an electrolyte (1 M LiPF<sub>6</sub> in FEC/FDEC/HFE) with different amounts of LiDFOB additives (0.00, 0.02, and 0.05 M). We found that the specific capacity of Li||LiCoMnO<sub>4</sub> cells increased with the additive amount, and the highest cycle stability was achieved in electrolytes with 0.02 M LiDFOB additives (Figure S19). As shown in Figure S20, the potential hysteresis between charging and discharging increased with the charge-discharge cycles in the LiDFOB-free electrolyte, whereas the charge-discharge potentials were much stable when 2% of LiDFOB was added into the electrolyte as a result of the formation of more robust CEI layer on the cathode. As shown in Figure S19, the capacity retention of the battery with 5% LiDFOB was a little lower than that of the battery with 2% additive as a result of the thicker interface film on the cathode in the electrolyte with 5% LiDFOB. As shown in Figure S21, the CEI layer on LiCoMnO<sub>4</sub> after 100 cycles in the electrolyte with 5% LiDFOB additive was around 8 nm, which is much thicker than that (4 nm) of CEI in the electrolyte with only 2% LiDFOB. Thick CEI will increase the interphase resistance (Figure S21D), resulting in capacity decay of the battery. In addition, the first discharge curves and corresponding dQ/dV profiles of LiCoMnO<sub>4</sub> cathodes in electrolytes with 0.02 M LiDFOB additive showed a small shoulder (Figure S20B) and a peak (Figure S20D) between 3.3 and 3.0 V (Figure S20B), which could be attributed to Li<sub>2</sub>MnO<sub>3</sub>.<sup>39</sup> However, it disappeared in the 50<sup>th</sup> and 100<sup>th</sup> discharge profiles as a result of the poor cycle stability of Li<sub>2</sub>MnO<sub>3</sub>.

The reason for high oxidation stability of the Li||LiCoMnO<sub>4</sub> cell in high-voltage all-fluorinated electrolyte can be attributed to the following:

- (1) Stable solvent: the fluorinated solvents (FEC, FDEC, and HFE) have high oxidation potentials as a result of the strong electron-withdrawing effect of the fluorine atom. Among them, the HFE component had the highest oxidation stability.
- (2) Stable CEI on LiCoMnO<sub>4</sub> cathode: all-fluorinated electrolyte formulation ensures that the highly fluorinated interphase with maximum protection power be formed when the electrolytes are oxidized, in which all components

(solvents [FEC, FDEC, and HFE] and salt anions [LiPF<sub>6</sub> and LiDFOB]) that are likely to be involved in interphase formation chemistry contain at least one fluorine in its structure. During the cycling, this high-voltage all-fluorinated electrolyte can contribute rich F-containing building blocks instead of evolving CO<sub>2</sub>, as is often observed for the traditional carbonate electrolytes, which is the very key issue for a stable CEI.

Furthermore, the Li||LiCoMnO<sub>4</sub> cell also delivers a high rate performance, retaining a capacity of 80 mAh g<sup>-1</sup> at a high rate of 2 A g<sup>-1</sup> (an approximately 25C rate calculated on the basis of the real test time) (Figure S22). The high rate capability of Li||LiCoMnO<sub>4</sub> cells is attributed to the three-dimensional ion diffusion pathways, solid-solution reaction mechanism in LiCoMnO<sub>4</sub>, and nanosize of the primary LiCoMnO<sub>4</sub> particles. We also investigated the self-discharge behaviors of Li||LiCoMnO<sub>4</sub> cells in high-voltage all-fluorine electrolyte and in FEC-based electrolyte. Figure S23 shows that the discharge capacity of Li||LiCoMnO<sub>4</sub> cells in all-fluorine electrolyte after 1 day, 1 week, and 1 month of rest can still maintain 83.8%, 70.4%, and 60.1%, respectively, of the discharge capacity of Li||LiCoMnO<sub>4</sub> cells with 10 min of rest. In sharp contrast, Li||LiCoMnO<sub>4</sub> cell after only 1 day of rest in FEC-based electrolyte (LiPF<sub>6</sub> in FEC/DMC) can maintain only 42% of the discharge capacity of Li||LiCoMnO<sub>4</sub> cells with 10 min of rest. It should be pointed out that 1 M LiPF<sub>6</sub> in FEC/FDEC/HFE/LiDFOB electrolyte with a wide voltage window is also compatible with the commercial PVDF binder and the carbon black, as demonstrated by a stable cycling performance (Figure S24). The good electrochemical performance was also demonstrated in the Li||LiCoMnO<sub>4</sub> cell with LiPAA as a binder in the cathode, which further confirmed that the enhanced electrochemical results were not due to the fluorinated binder (Figure S25).

#### *Electrochemical Performance of a 5.2 V Graphite||LiCoMnO<sub>4</sub> Cell*

Figure 6A shows the galvanostatic charge-discharge profiles of the graphite at different cycles in the electrolyte (1 M LiPF<sub>6</sub> + 0.02 M LiDFOB in FEC/FDEC/HFE). Graphite delivered approximately 300 mAh g<sup>-1</sup> reversible capacity at the current density of 0.1 A g<sup>-1</sup> with a 100% CE after the second cycle. Furthermore, the capacity exhibited almost no decay over 100 cycles (Figure 6C) and was retained at 90% over 300 cycles (Figure S26). This electrolyte also showed good stability to the graphite anode in addition to Li-metal anodes, which is totally different from other high voltage electrolytes, such as sulfone and organic nitrile electrolytes. As demonstrated by XPS analysis, the versatile electrolyte (1 M LiPF<sub>6</sub> + 0.02 M LiDFOB in FEC/FDEC/HFE) formed a LiF-rich SEI on graphite anodes. The LiF content in the SEI layer was as high as ~70% (Figure S27). The extremely low electronic conductivity of LiF significantly increased the stability of the SEI and enhanced the CE and cycle stability. Moreover, the graphite also delivered a good rate performance in this electrolyte (Figure S28).

Graphite||LiCoMnO<sub>4</sub> cells were fabricated at a LiCoMnO<sub>4</sub>/graphite weight ratio of 2:1 on the basis of the specific capacities of LiCoMnO<sub>4</sub> and graphite, 152 and 300 mAh g<sup>-1</sup>, respectively. The galvanostatic charge-discharge profiles of the graphite||LiCoMnO<sub>4</sub> cell at the rate of 1 C showed two sloping high voltage plateaus, from 4.9 to 5.3 V and 4.6 to 4.8 V, which provides a specific capacity of 100 mAh g<sup>-1</sup>, calculated on the basis of total active materials of both the LiCoMnO<sub>4</sub> cathode and graphite anode (Figure 6B). The high operating voltage and high capacity of graphite||LiCoMnO<sub>4</sub> cells ensure a high energy density of 480 Wh kg<sup>-1</sup> with an excellent cycle stability of 90% capacity retention after 100 cycles (Figure 6D). In addition, we also extended the cycle performance of this high-voltage LIB at a low rate of 0.1C, which also delivered very stable cycle stability with a CE ~ 99%



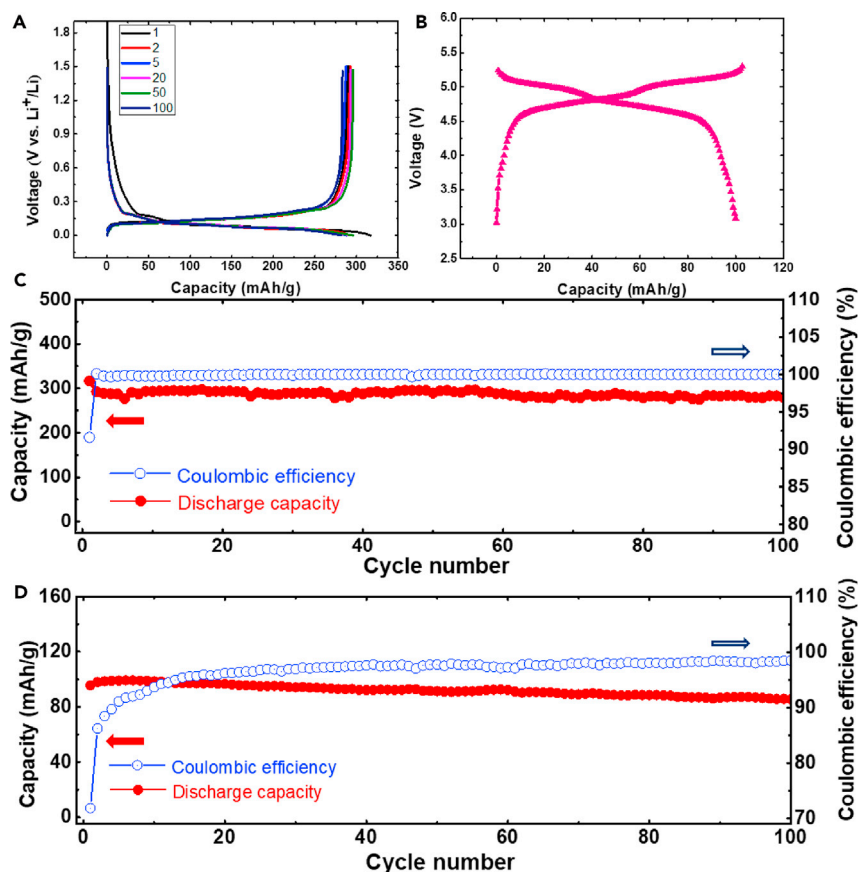


**Figure 6. Electrochemical Performance of the Graphite||LiCoMnO<sub>4</sub> Battery**

(A) Galvanostatic charge-discharge profiles of graphite with different cycles at a current density of 0.1 A g<sup>-1</sup> (calculated on the basis of the activated material) between 0 and 1.5 V in the electrolyte 1 M LiPF<sub>6</sub> + 0.02 M LiDFOB in FEC/FDEC/HFE.

(B) Typical galvanostatic charge-discharge profile of the graphite||LiCoMnO<sub>4</sub> Li-ion battery at the current rate of 1 C (1 h for the charge or discharge process) with the electrolyte 1 M LiPF<sub>6</sub> + 0.02 M LiDFOB in FEC/FDEC/HFE within the voltage window of 3–5.3 V.

(C) Cycle performance of the graphite at a current density of 0.1 A g<sup>-1</sup> (calculated on the basis of the activated material) between 0 and 1.5 V in the electrolyte 1 M LiPF<sub>6</sub> + 0.02 M LiDFOB in FEC/FDEC/HFE.

(D) Cycle performance of the graphite||LiCoMnO<sub>4</sub> Li-ion battery at the current rate of 1 C (1 h for the charge or discharge process) with the electrolyte 1 M LiPF<sub>6</sub> + 0.02 M LiDFOB in FEC/FDEC/HFE within the voltage window of 3–5.3 V.

(Figure S29). Compared with other battery chemistries, especially the intensively investigated Ni-rich cathode-based cells, LiCoMnO<sub>4</sub> possesses better thermal stability because of its stable spinel structure.<sup>47</sup> In addition, this electrolyte (1 M LiPF<sub>6</sub> + 0.02 M LiDFOB in FEC/FDEC/HFE) is non-flammable.<sup>22</sup> Therefore, the graphite||LiCoMnO<sub>4</sub> and Li||LiCoMnO<sub>4</sub> metal cells provided here are much safer than other Ni-based Li battery systems. Moreover, batteries with a higher operation voltage tend to have a higher power capability,<sup>47</sup> enabling them to be more suitable for EVs.

## EXPERIMENTAL PROCEDURES

### Synthesis and Characterization of LiCoMnO<sub>4</sub>

LiCoMnO<sub>4</sub> was synthesized by an original two-step method. The first step was the synthesis of MnCoO<sub>x</sub>. First, 2.10 mmol CoCl<sub>2</sub>·6H<sub>2</sub>O plus 1.75 mmol MnCl<sub>2</sub>·4H<sub>2</sub>O

was dissolved in 66 mL of distilled water, and 2.460 g of urea, 2.500 g of ascorbic acid, and 2.000 g of polyvinylpyrrolidone (molecular weight  $\sim 40K$ ) were then added to the  $\text{CoCl}_2/\text{MnCl}_2$  solution in sequence under stirring for 1 h. After being stirred for 1 h, the solution was transferred to a 100 mL Teflon-lined stainless-steel autoclave and maintained at  $160^\circ\text{C}$  for 6 h. The  $\text{CoMnCO}_3$  microspheres were obtained after being centrifuged, washed with water and ethanol several times, and dried at  $60^\circ\text{C}$  overnight. The obtained  $\text{CoMnCO}_3$  microspheres were calcinated in air at  $400^\circ\text{C}$  for 5 h to obtain the  $\text{CoMnO}_x$  microspheres. Then, 0.700 g of  $\text{CoMnO}_x$  and 0.165 g of  $\text{Li}_2\text{CO}_3$  were mixed and calcinated at  $800^\circ\text{C}$  for 24 h in an  $\text{O}_2$  atmosphere to obtain the  $\text{LiCoMnO}_4$  product.

### XRD and Refinements

*Ex situ* and *in situ* XRD experiments were performed at the 28-ID-2 beamline of the National Synchrotron Light Source II (NSLS II) at Brookhaven National Laboratory (BNL) with a Perkin Elmer amorphous-Si flat panel detector. For *in situ* XRD, the *in situ* cell was made by assembling active material, carbon black, and PTFE binder into a pouch cell. The pouch cell was then sandwiched by two metallic plates with a carbon window in the center, guaranteeing pressure on the cell. Collected raw image data were then integrated to yield the 2 $\theta$ -intensity XRD pattern with the software Fit2D.<sup>48</sup> Rietveld refinement<sup>49</sup> was carried out with GSAS-EXPGUI software.<sup>50,51</sup>

### SEM and TEM

The morphologies of the sample were examined using a Hitachi SU-70 field-emission scanning electron microscope and a JEOL 2100F field emission transmission electron microscope.

### HRTEM and HAADF-STEM

The experiment was performed using a JEOL 2010F transmission electron microscope operating at an accelerating voltage of 200 kV. HAADF-STEM and STEM electron energy loss spectroscopy (EELS) were performed with an aberration-corrected Hitachi HD 2700C STEM at 200 kV in Brookhaven National Lab. The conversion angle and collection angles for STEM imaging were 22 and 64–341 mrad, respectively.

### XPS

The surface chemistry of the electrodes after cycling was examined by XPS with a Kratos Axis 165 spectrometer. The electrodes were then removed from the cell after 100 cycles and rinsed with DMC inside a glove box three times. All samples were dried under vacuum overnight, placed in a sealed bag, and then transferred into the XPS chamber under inert conditions in an argon-filled glove bag. XPS data were collected using a monochromated Al  $K\alpha$  X-ray source (1,486.7 eV). The working pressure of the chamber was lower than  $6.6 \times 10^{-9}$  Pa. All reported binding energy values were calibrated to the C 1s peak at 284.8 eV.

### XANES and EXAFS

XAS measurements were performed at the 12BM beamline of the Advanced Photon Sources at Argonne National Laboratory in transmission mode. The XANES and EXAFS spectra were processed with the Athena software package<sup>52</sup> The AUTOBK code was used to normalize the absorption coefficient and separate the EXAFS signal,  $\chi(k)$ , from the isolated atom-absorption background. The extracted EXAFS signal,  $\chi(k)$ , was weighted by  $k^3$  to emphasize the high-energy oscillations and then Fourier transformed in a  $k$  range from 3.0 to  $13.5 \text{ \AA}^{-1}$  for analyzing the data in R space.

### Electrode Preparation and Electrochemical Measurements

To prepare the working electrode, the as-synthesized  $\text{LiCoMnO}_4$  and other commercial cathodes ( $\text{LiCoPO}_4$  and  $\text{LiNi}_{0.5}\text{Mn}_{1.5}\text{O}_4$ ), anode materials (graphite and MCMB purchased from MTI) mixed with carbon black, and PVDF or LiPAA with a mass ratio of 80:10:10 were ground into a homogeneous slurry in *N*-methyl-2-pyrrolidone or  $\text{H}_2\text{O}$  with a mortar and pestle. The slurry mixture was coated onto Al or Cu foil and then dried at  $100^\circ\text{C}$  for 12 h. The loading mass of the active materials for the electrode was approximately  $1\text{ mg/cm}^2$  (for the electrodes for *ex situ* XANES, *ex situ* EXAFS, and *in situ* XRD were  $8\text{ mg/cm}^2$ ). The all-fluorinated electrolyte solution comprised 1 M  $\text{LiPF}_6$  in FEC/FDEC/HFE (2:6:2 by volume) with different amounts of additives (without or with 0.02 or 0.05 M LiDFOB). The conventional electrolyte solution comprised 1 M  $\text{LiPF}_6$  in EC/DMC (1:1 by volume). The FEC-based electrolyte solution comprised 1 M  $\text{LiPF}_6$  in FEC/DMC (2:8 by volume). The cells were assembled with a polypropylene microporous film (Celgard 3501) as the separator. The electrochemical tests were performed with a coin-type half cell (CR 2016), which was fabricated in a glove box filled with argon. Electrochemical performance was tested with an Arbin battery test station (BT2000, Arbin Instruments, USA).

### SUPPLEMENTAL INFORMATION

Supplemental Information can be found with this article online at <https://doi.org/10.1016/j.chempr.2019.02.003>.

### ACKNOWLEDGMENTS

This work was supported by the US Department of Energy (DOE) under awards DEEE0008200 and DEEE0008202. E.H. and X.Y. were supported by the Assistant Secretary for Energy Efficiency and Renewable Energy, Vehicle Technology Office of the US Department of Energy through the Advanced Battery Materials Research Program, including Battery500 Consortium under contract DE-SC0012704. This research used beamlines 7-BM of the National Synchrotron Light Source II, a DOE Office of Science User Facility operated for the DOE Office of Science by Brookhaven National Laboratory under contract DE-SC0012704. Electron microscopy work was performed at the Center for Functional Nanomaterials of the Brookhaven National Laboratory, which is supported by the DOE Office of Basic Energy Sciences under contract DE-SC0012704.

### AUTHOR CONTRIBUTIONS

L.C. and X.F. designed the experiments, analyzed data, and wrote the paper. X.J., J.C., S.H., and T.D. conducted the experiments. E.H. and X.Y. conducted the *in situ* XRD, XANES, and EXAFS tests and corresponding data analysis. J.L. and D.S. conducted the HRTEM and HR-HAADF-STEM tests and corresponding data analysis. C.W. conceived and supervised the project. All authors contributed to the interpretation of the results.

### DECLARATION OF INTERESTS

The authors declare no competing interests.

Received: September 13, 2018

Revised: November 5, 2018

Accepted: February 5, 2019

Published: February 28, 2019

## REFERENCES AND NOTES

- Luo, K., Roberts, M.R., Hao, R., Guerrini, N., Pickup, D.M., Liu, Y.S., Edström, K., Guo, J., Chadwick, A.V., Duda, L.C., et al. (2016). Charge-compensation in 3rd-transition-metal-oxide intercalation cathodes through the generation of localized electron holes on oxygen. *Nat. Chem.* 8, 684–691.
- Seo, D.H., Lee, J., Urban, A., Malik, R., Kang, S., and Ceder, G. (2016). The structural and chemical origin of the oxygen redox activity in layered and cation-disordered Li-excess cathode materials. *Nat. Chem.* 8, 692–697.
- Sathiyar, M., Rousse, G., Ramesha, K., Laissa, C.P., Vezin, H., Sougrati, M.T., Doublet, M.L., Foix, D., Gonbeau, D., Walker, W., et al. (2013). Reversible anionic redox chemistry in high-capacity layered-oxide electrodes. *Nat. Mater.* 12, 827–835.
- Pan, H., Chen, J., Cao, R., Murugesan, V., Rajput, N.N., Han, K.S., Persson, K., Estevez, L., Engelhard, M.H., Zhang, J., et al. (2017). Non-encapsulation approach for high-performance Li-S batteries through controlled nucleation and growth. *Nat. Energy* 2, 813–820.
- Maitra, U., House, R.A., Somerville, J.W., Tapiar-Ruiz, N., Lozano, J.G., Guerrini, N., Hao, R., Luo, K., Jin, L., Pérez-Osorio, M.A., et al. (2018). Oxygen redox chemistry without excess alkali-metal ions in  $\text{Na}_{2/3}[\text{Mg}_{0.28}\text{Mn}_{0.72}]\text{O}_2$ . *Nat. Chem.* 10, 288–295.
- Choi, J.W., and Aurbach, D. (2016). Promise and reality of post-lithium-ion batteries with high energy densities. *Nat. Rev. Mater.* 1, 1–16.
- Bruce, P.G., Freunberger, S.A., Hardwick, L.J., and Tarascon, J.M. (2011). Li-O<sub>2</sub> and Li-S batteries with high energy storage. *Nat. Mater.* 11, 19–29.
- Li, W., Song, B., and Manthiram, A. (2017). High-voltage positive electrode materials for lithium-ion batteries. *Chem. Soc. Rev.* 46, 3006–3059.
- Hu, M., Pang, X., and Zhou, Z. (2013). Recent progress in high-voltage lithium ion batteries. *J. Power Sources* 237, 229–242.
- Julien, C.M., and Mauger, A. (2013). Review of 5-V electrodes for Li-ion batteries: status and trends. *Ionics* 19, 951–988.
- Wu, F., and Yushin, G. (2017). Conversion cathodes for rechargeable lithium and lithium-ion batteries. *Energy Environ. Sci.* 10, 435–459.
- Huggins, R.A. (1996). Transient behavior of insertion reaction electrodes. *Solid State Ion* 86–88, 41–48.
- Suo, L., Xue, W., Gobet, M., Greenbaum, S.G., Wang, C., Chen, Y., Yang, W., Li, Y., and Li, J. (2018). Fluorine-donating electrolytes enable highly reversible 5-V-class Li metal batteries. *Proc. Natl. Acad. Sci. USA* 115, 1156–1161.
- Yang, L., Ravdel, B., and Luchta, B.L. (2010). Electrolyte reactions with the surface of high voltage  $\text{LiNi}_{0.5}\text{Mn}_{1.5}\text{O}_4$  cathodes for lithium-ion batteries. *Electrochem. Solid State Lett.* 13, A95–A97.
- Hu, L., Zhang, Z., and Amine, K. (2013). Electrochemical investigation of carbonate-based electrolytes for high voltage lithium-ion cells. *J. Power Sources* 236, 175–180.
- Kawai, H., Nagata, M., Tukamoto, H., and Westa, A.R. (1998). A new lithium cathode  $\text{LiCoMnO}_4$ : Toward practical 5 V lithium batteries. *Electrochem. Solid State Lett.* 1, 212–214.
- Mandal, S., Rojas, R.M., Amarilla, J.M., Calle, P., Kosova, N.V., Anufrienko, V.F., and Rojo, J.M. (2002). High temperature co-doped  $\text{LiMn}_2\text{O}_4$ -based spinels. Structural, electrical, and electrochemical characterization. *Chem. Mater.* 14, 1598–1605.
- Kawata, H., Nagata, M., Kageyama, H., Tukamoto, H., and West, A.R. (1999). 5 V lithium cathodes based on spinel solid solutions  $\text{Li}_2\text{Co}_{1-x}\text{Mn}_{3-x}\text{O}_8$ :  $-1 \leq x \leq 1$ . *Electrochim. Acta* 45, 315–327.
- Abouimrane, A., Belharouak, I., and Amine, K. (2009). Sulfone-based electrolytes for high-voltage Li-ion batteries. *Electrochem. Commun.* 11, 1073–1076.
- Xu, K., and Angell, C.A. (2002). Sulfone-based electrolytes for lithium-ion batteries. *J. Electrochem. Soc.* 149, A920–A926.
- Yamada, Y., Furukawa, K., Sodeyama, K., Kikuchi, K., Yaegashi, M., Tateyama, Y., and Yamada, A. (2014). Unusual stability of acetonitrile-based superconcentrated electrolytes for fast-charging lithium-ion batteries. *J. Am. Chem. Soc.* 136, 5039–5046.
- Hu, L., Zhang, Z., and Amine, K. (2013). Fluorinated electrolytes for Li-ion battery: an FEC-based electrolyte for high voltage  $\text{LiNi}_{0.5}\text{Mn}_{1.5}\text{O}_4$ /graphite couple. *Electrochem. Commun.* 35, 76–79.
- Zhang, Z., Hu, L., Wu, H., Weng, W., Koh, M., Redfern, P.C., Curtiss, L.A., and Amine, K. (2013). Fluorinated electrolytes for 5 V lithium-ion battery chemistry. *Energy Environ. Sci.* 6, 1806–1810.
- Markevich, E., Salitra, G., and Aurbach, D. (2017). Fluoroethylene carbonate as an important component for the formation of an effective solid electrolyte interphase on anodes and cathodes for advanced Li-ion batteries. *ACS Energy Lett.* 2, 1337–1345.
- Zhu, Y., Li, Y., Bettge, M., and Abraham, D.P. (2012). Positive electrode passivation by LiDFOB electrolyte additive in high-capacity lithium-ion cells. *J. Electrochem. Soc.* 159, A2109–A2117.
- Wu, Q., Lu, W., Miranda, M., Honaker-Schroeder, T.K., Lakhsassi, K.Y., and Dees, D. (2012). Effects of lithium difluoro(oxalate) borate on the performance of Li-rich composite cathode in Li-ion battery. *Electrochem. Commun.* 24, 78–81.
- Cha, J., Han, J., Hwang, J., Cho, J.C., and Choi, N. (2017). Mechanisms for electrochemical performance enhancement by the salt-type electrolyte additive, lithium difluoro(oxalato) borate, in high-voltage lithium-ion batteries. *J. Power Sources* 357, 97–106.
- Kaneko, Y., Park, J., Yokotsuji, H., Odawara, M., Takase, H., Ue, M., and Lee, M. (2016). Cathode solid electrolyte interface's function originated from salt type additives in lithium ion batteries. *Electrochim. Acta* 222, 271–279.
- Windmüller, A., Tsai, C., Möller, S., Balski, M., Sohn, Y.J., Uhlenbruck, S., and Guillon, O. (2017). Enhancing the performance of high-voltage  $\text{LiCoMnO}_4$  spinel electrodes by fluorination. *J. Power Sources* 341, 122–129.
- Huang, X., Lin, M., Tong, Q., Li, X., Ruan, Y., and Yang, Y. (2012). Synthesis of  $\text{LiCoMnO}_4$  via a sol-gel method and its application in high power  $\text{LiCoMnO}_4/\text{Li}_4\text{Ti}_5\text{O}_{12}$  lithium-ion batteries. *J. Power Sources* 202, 352–356.
- Alcántara, R., Jaraba, M., Lavela, P., and Tirado, J.L. (2003). Electrochemical, <sup>6</sup>Li MAS NMR, and X-ray and neutron diffraction study of  $\text{LiCo}_x\text{Fe}_y\text{Mn}_{2-(x+y)}\text{O}_4$  spinel oxides for high-voltage cathode materials. *Chem. Mater.* 15, 1210–1216.
- Hu, M., Tian, Y., Su, L., Wei, J., and Zhou, Z. (2013). Preparation and Ni-doping effect of nanosized truncated octahedral  $\text{LiCoMnO}_4$  as cathode materials for 5 V Li-ion batteries. *ACS Appl. Mater. Interfaces* 5, 12185–12189.
- Hu, M., Tian, Y., Wei, J., Wang, D., and Zhou, Z. (2014). Porous hollow  $\text{LiCoMnO}_4$  microspheres as cathode materials for 5 V lithium ion batteries. *J. Power Sources* 247, 794–798.
- Dräger, C., Sigel, F., Indris, S., Mikhailova, D., Pfaffmann, L., Knapp, M., and Ehrenberg, H. (2017). Delithiation/re-lithiation process of  $\text{LiCoMnO}_4$  spinel as 5 V electrode material. *J. Power Sources* 371, 55–64.
- Ariyoshi, K., Yamamoto, H., and Yamada, Y. (2018). High dimensional stability of  $\text{LiCoMnO}_4$  as positive electrodes operating at high voltage for lithium-ion batteries with a long cycle life. *Electrochim. Acta* 260, 498–503.
- Zhang, Q., Pan, J., Lu, P., Liu, Z., Verbrugge, M.W., Sheldon, B.W., Cheng, Y.T., Qi, Y., and Xiao, X. (2016). Synergistic effects of inorganic components in solid electrolyte interphase on high cycle efficiency of lithium ion batteries. *Nano Lett.* 16, 2011–2016.
- Lu, Y., Tu, Z., and Archer, L.A. (2014). Stable lithium electrodeposition in liquid and nanoporous solid electrolytes. *Nat. Mater.* 13, 961–969.
- Nam, K.W., Bak, S., Hu, E., Yu, X., Zhou, Y., Wang, X., Wu, L., Zhu, Y., Chung, K., and Yang, X. (2013). Combining in situ synchrotron X-ray diffraction and absorption techniques with transmission electron microscopy to study the origin of thermal instability in overcharged cathode materials for lithium-ion batteries. *Adv. Funct. Mater.* 23, 1047–1063.
- Rana, J., Stan, M., Kloepsch, R., Li, J., Schumacher, G., Welter, E., Zizak, I., Banhart, J., and Winter, M. (2014). Structural changes in  $\text{Li}_2\text{MnO}_3$  cathode material for Li-ion batteries. *Adv. Energy Mater.* 4, 1300998.
- Chen, H., and Islam, M.S. (2016). Lithium extraction mechanism in Li-Rich  $\text{Li}_2\text{MnO}_3$  involving oxygen hole formation and dimerization. *Chem. Mater.* 28, 6656–6663.
- Matsunaga, T., Komatsu, H., Shimoda, K., Minato, T., Yonemura, M., Kamiyama, T., Kobayashi, S., Kato, T., Hirayama, T., Ikuhara,

- Y., et al. (2016). Dependence of structural defects in  $\text{Li}_2\text{MnO}_3$  on synthesis temperature. *Chem. Mater* 28, 4143–4150.
42. Lyu, Y., Zhao, N., Hu, E., Xiao, R., Yu, X., Gu, L., Yang, X., and Li, H. (2015). Probing reversible multielectron transfer and structure evolution of  $\text{Li}_{1.2}\text{Cr}_{0.4}\text{Mn}_{0.4}\text{O}_2$  cathode material for Li-ion batteries in a voltage range of 1.0–4.8 V. *Chem. Mater* 27, 5238–5252.
43. Ammundsen, B., Jones, D.J., Rozière, J., and Burns, G.R. (1996). Effect of chemical extraction of lithium on the local structure of spinel lithium manganese oxides determined by X-ray absorption spectroscopy. *Chem. Mater* 8, 2799–2808.
44. Zhecheva, E., Stoyanova, R., Alcántara, R., Lavela, P., and Tirado, J.L. (2006). EPR studies of Li deintercalation from  $\text{LiCoMnO}_4$  spinel-type electrode active material. *J. Power Sources* 159, 1389–1394.
45. Shannon, R.D. (1976). Revised effective ionic radii and systematic studies of interatomic distances in halides and Chalcogenides. *Acta Crystallogr. A* 32, 751–767.
46. Qian, J., Henderson, W.A., Xu, W., Bhattacharya, P., Engelhard, M., Borodin, O., and Zhang, J.G. (2015). High rate and stable cycling of lithium metal anode. *Nat. Commun* 6, 6362.
47. Bruke, A., and Miller, M. (2009). Performance characteristics of lithium-ion batteries of various chemistries for plug-in hybrid vehicles. In *Proceedings of the 24<sup>th</sup> International Battery, Hybrid and Fuel Cell Electric Vehicle Symposium (EVS24)*, pp. 1–13.
48. Hammersley, A.P., Svensson, S.O., Hanfland, M., Fitch, A.N., and Hausermann, D. (1996). Two-dimensional detector software: from real detector to idealised image or two-theta scan. *High Press. Res.* 14, 235–248.
49. Rietveld, H.M. (1969). A profile refinement method for nuclear and magnetic structures. *J. Appl. Crystallogr* 2, 65–71.
50. Larson, A.C., and Von Dreele, R.B. (2004). General Structure Analysis System (GSAS). In *Los Alamos National Laboratory Report LAUR 86-748*. <https://11bm.xray.aps.anl.gov/documents/GSASManual.pdf>.
51. Toby, B.H. (2001). EXPGUI, a graphical user interface for GSAS. *J. Appl. Crystallogr* 34, 210–213.
52. Ravel, B., and Newville, M. (2005). ATHENA, Artemis, Hephaestus: Data analysis for X-ray absorption spectroscopy using IFEFFIT. *J. Synchrotron Radiat* 12, 537–541.